Theory based scaling of edge turbulence and implications for the scrape-off layer width

J. R. Myra, D. A. Russell, and S. J. Zweben

Citation: Physics of Plasmas **23**, 112502 (2016); doi: 10.1063/1.4966564
View online: http://dx.doi.org/10.1063/1.4966564
View Table of Contents: http://scitation.aip.org/content/aip/journal/pop/23/11?ver=pdfcov
Published by the AIP Publishing

Theory based scaling of edge turbulence and implications for the scrape-off layer width

J. R. Myra,[1] D. A. Russell,[1] and S. J. Zweben[2]
[1]*Lodestar Research Corporation, 2400 Central Avenue, Boulder, Colorado 80301, USA*
[2]*Princeton Plasma Physics Laboratory, Princeton, New Jersy 08540, USA*

(Received 24 May 2016; accepted 16 October 2016; published online 1 November 2016)

Turbulence and plasma parameter data from the National Spherical Torus Experiment (NSTX) [Ono *et al.*, Nucl. Fusion **40**, 557 (2000)] is examined and interpreted based on various theoretical estimates. In particular, quantities of interest for assessing the role of turbulent transport on the midplane scrape-off layer heat flux width are assessed. Because most turbulence quantities exhibit large scatter and little scaling within a given operation mode, this paper focuses on length and time scales and dimensionless parameters between operational modes including Ohmic, low (L), and high (H) modes using a large NSTX edge turbulence database [Zweben *et al.*, Nucl. Fusion **55**, 093035 (2015)]. These are compared with theoretical estimates for drift and interchange rates, profile modification saturation levels, a resistive ballooning condition, and dimensionless parameters characterizing L and H mode conditions. It is argued that the underlying instability physics governing edge turbulence in different operational modes is, in fact, similar, and is consistent with curvature-driven drift ballooning. Saturation physics, however, is dependent on the operational mode. Five dimensionless parameters for drift-interchange turbulence are obtained and employed to assess the importance of turbulence in setting the scrape-off layer heat flux width λ_q and its scaling. An explicit proportionality of the width λ_q to the safety factor and major radius (qR) is obtained under these conditions. Quantitative estimates and reduced model numerical simulations suggest that the turbulence mechanism is not negligible in determining λ_q in NSTX, at least for high plasma current discharges. *Published by AIP Publishing.* [http://dx.doi.org/10.1063/1.4966564]

I. INTRODUCTION

A topic of great contemporary interest for tokamak magnetic fusion research is the possible role of edge turbulence in influencing the scrape-off layer (SOL) heat flux width. More generally, edge turbulence is both driven by, and in part determines, plasma and flow profiles throughout the edge region, setting the conditions for low (L) and high (H) mode confinement that are critical to understand for the success of fusion. These considerations motivate fundamental studies of the character of tokamak edge and SOL turbulence and their linkages to the transport of particles and heat across the last closed flux surface.

Many papers have been written on edge and SOL turbulence, including recent reviews,[1–4] the latter two of which specifically address the topic of blob-filaments in the SOL. The complexity of the edge region in general, and turbulence in particular, has been a limiting factor for the applicability of both analytical and numerical models. Ideally, theory-based relationships for interpreting experimental turbulence data are desired. There have been a few attempts in this direction.

A phase space regime diagram based on drift-resistive ballooning was proposed[5] and applied to Alcator C-Mod experimental data.[6] SOL transport and regime transitions were linked with collisionality and theory-based estimates for ASDEX-Upgrade experiments.[7] Parametric dependences of the L to H transition threshold have been related to turbulence properties.[8] Statistical properties of SOL turbulence in the TCV tokamak, such as distributions of amplitude and waiting times, have been very successfully described by a statistical model.[9] Analytical scalings of blob velocities[3] were compared with metadata from a number of experiments.[4] More recent attempts at comparing tokamak experimental blob velocities with analytical scalings and regimes have also been carried out.[10–14] Scaling of edge turbulence and transport properties based on an international database were carried out in Ref. 15 which emphasized a strong connection between drift wave turbulence in the edge and blobs in the SOL. In addition to papers which have addressed the scaling of edge turbulence with parameter variations, there are a large number of papers in which numerical modeling of turbulence in specific discharges has been advanced; some have specifically addressed the SOL heat flux width question.[16–25]

In general, although edge and SOL turbulence data in tokamaks is order-of-magnitude consistent with theoretical expectations for length and time scales, clean parametric scaling dependences have often been elusive. This point is evident from recently published data from the National Spherical Torus Experiment (NSTX)[26] as described in the analysis of a large edge turbulence database.[10] Data for turbulence length and time scales within a particular operational mode, Ohmic, L or H mode, generally shows far more scatter than scaling. This may be partly due to the fact that plasma parameters could vary considerably between one coherent structure (blob) and another in the same discharge. As well, there are turbulent variations in the background plasma

through which the structures propagate. Such variations could make it difficult to extract scaling with global or even local time-averaged parameters of the discharge. Furthermore, within a given operational mode, the accessible range of parameter variations in a given device is limited.

In this paper, we make the ansatz that the *physical processes* underlying edge-SOL instabilities in all operational modes are similar enough to justify a search for parametric scalings *between* operation modes. Indeed, blob structures emitted in L and H mode plasmas appear qualitatively similar in character (though not in number or amplitude).[10,11] We will examine relationships between the mean values of various edge turbulence database quantities in four operational modes: Ohmic (OH), low (L), low with applied rf (L-RF), and high (H). Here regular L mode refers to neutral beam heated plasmas, while the L-RF plasmas were heated by high harmonic fast waves.

It will be evident from Refs. 10 and 11 that much edge turbulence data is at best only understood qualitatively. While it is important to keep that perspective in mind, we show in this paper, that a few carefully selected properties of the turbulence exhibit reasonable quantitative scaling behavior among different operational modes. Of particular interest are the scaling of the typical wavenumbers and frequencies, and the character of the underlying instabilities. The main goal of the present paper is to investigate these scaling properties of the turbulence and apply them to the problem of turbulent transport in the near SOL. Our paper thus extends previously published results which surveyed a broad scope of turbulence observations from the large database,[10] and specifically for tracked blobs, from the subset database.[11] Two results from Ref. 10 are recapitulated here for continuity of the present analysis.

Recently, the role of turbulent transport in setting the SOL heat flux width λ_q was assessed using heuristic arguments.[27] The analysis begins with the estimate $q_\perp/\lambda_q \approx q_{||}/L_{||}$ where $q_\perp$ is the turbulent heat flux flowing across the separatrix, $q_{||}$ is the heat flux flowing down the SOL exhaust channel, and $L_{||}$ is the field line length. Estimating $L_{||} \approx qR$ where q is the safety factor (e.g., at the 95% flux surface) and R is the major radius, and defining an effective parallel energy transmission factor $g = q_{||}/(pc_s)$ where c_s is the ion sound speed, and p is the plasma pressure at the separatrix, one obtains the general result

$$\lambda_q \approx \frac{qR}{g}\frac{q_\perp}{pc_s} = \frac{qR}{g}\frac{\langle \tilde{p}\,\tilde{v}_x\rangle}{pc_s}. \quad (1)$$

Here $\tilde{v}_x$ is the perturbed $E \times B$ velocity in the radial (x) direction, and $\tilde{p}$ is the perturbed pressure. The physics governing the parallel heat flow factor qR/g is relatively well understood and believed to be governed by classical transport. Of interest here is understanding what NSTX edge turbulence data can tell us about the $q_\perp/(pc_s)$ factor.

It is possible to proceed from Eq. (1) to a scaling for λ_q in terms of q, R, $\rho_s = c_s/\Omega_i$ and other parameters once the dispersion character, spatial scales and saturation levels of the turbulence are known. This was approached theoretically in Ref. 27 using several different models for the instabilities, saturation, and turbulent transport physics. Here we address the same questions by data analysis. This is followed by a discussion of scaling implications for the SOL width based on the properties of the turbulence that are revealed by that analysis and by a numerical simulation. Understanding and characterizing the scaling of the SOL heat flux width is an ongoing major effort in the international fusion community. Recent empirical multi-machine fits have been presented for both diverted H mode[28] and inner-wall-limited L mode[29] discharges.

The work presented here and in Ref. 27 is also related to previous well-known analyses of the SOL widths by Connor[30] and Counsell,[31] which compared the predictions of a large number of theoretical models with data from several experiments. Those analyses asked whether broad data scans support particular types of models rather than attempting to take into account theoretical validity constraints or careful selection of data. It was concluded that models with drift wave or magneto-hydrodynamic (MHD) interchange character provide the best overall fits to cross-field transport in the SOL. This conclusion is consistent with the present more limited and more focused investigation. Here we take advantage of a large NSTX database in which turbulent quantities were measured, allowing us to investigate the underlying mechanisms more directly.

The plan of our paper is as follows. In Sec. II, a brief description of the experimental database is reviewed. Section III contains the main results for scaling properties between operational modes. Saturation levels, and other characteristics which differ between operational modes are considered in Sec. IV. Results are applied to the SOL heat flux width problem in the discussion of Sec. V. A reduced model numerical simulation is discussed in Sec. VI. Finally the summary and conclusions are given in Sec. VII.

II. THE EXPERIMENTAL DATABASE

The experimental database used for this analysis is the same as that described in detail in Ref. 10. It consists of a total of 140 NSTX discharges, 93 of which are in H mode, 9 in (neutral beam heated) L mode, 5 in (high harmonic fast wave heated) L-RF mode, and 33 in OH mode. In addition, the large database contains within it a high quality subset[11] consisting of 7 H modes and 7 OH modes, (denoted OH7 and H7) where each group of 7 has similar parameters and good Thomson scattering profiles for the electron density n_e and temperature T_e. The profiles and fits used in the analysis that follows are shown in Fig. 1. Scaling results for the subset database are indicated separately from the large database in Sections III and IV. For each operational mode in the subset database, density and electron pressure gradients were computed from the smooth fits, and these same gradients were used for all 7 discharges in the set. This procedure reduced uncertainties in the gradients compared to the large database where only single-discharge information was available.

The radial variation of a few characteristic frequencies of interest, as calculated from the smoothed profiles, are shown in Fig. 2. Here the characteristic frequencies are defined as

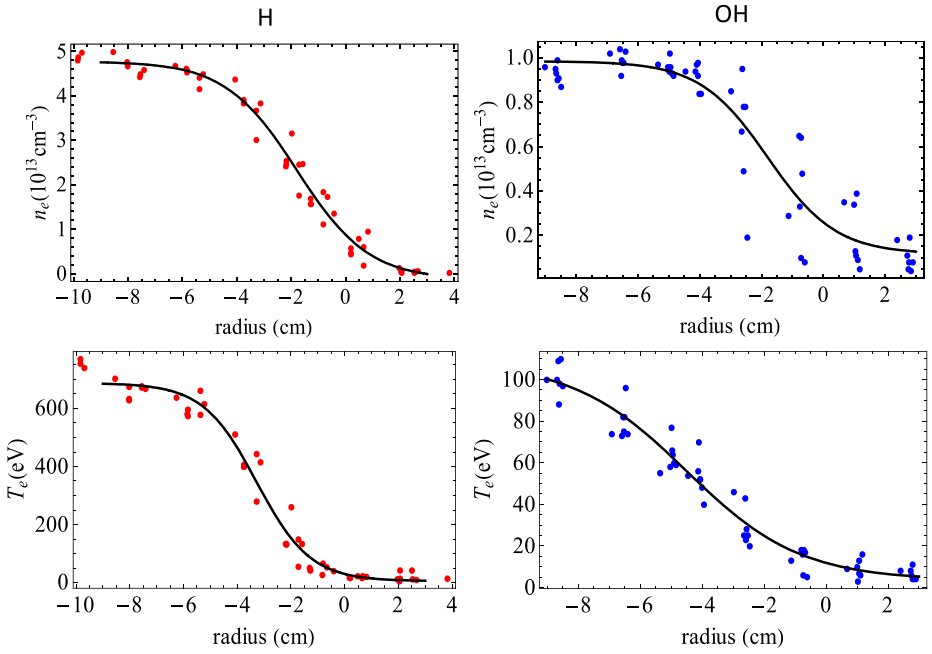

FIG. 1. Thomson scattering profile data vs. radius (relative to the EFIT separatrix) for the high quality subset database for H mode and Ohmic plasmas (small dots) and smooth fits (solid curves). For each case (H and OH) the data points are an ensemble of all seven similar discharges.

$$\gamma_{\mathrm{mhd}} = \frac{c_s}{\left(R\lambda_p\right)^{1/2}}, \tag{2}$$

$$\omega_* = \frac{k_y c_s \rho_s}{\lambda_p}, \tag{3}$$

$$V'_y = \frac{d}{dr}V_E \approx -\frac{d}{dr}V_{di} \approx \frac{d}{dr}V_{de}, \tag{4}$$

where $c_s = (T_e/m_i)^{1/2}$, $\lambda_p = -p_e/(dp_e/dr)$, $\rho_s = c_s/\Omega_i$, $\Omega_i = eB/m_i c$, $V_E = -cE_r/B$ is the E × B drift in the radial electric field, and V_{di}, V_{de} are the diamagnetic drifts, $V_{di} = v_{ti}\rho_i/\lambda_{pi}$ and $V_{de} = c_s\rho_s/\lambda_{pe}$. In calculating ω_*, $k_y = 0.22$ and $0.35\,\mathrm{cm}^{-1}$ in H and OH, respectively, have been used (see Sec. III). Equation (4) is a very rough estimate of the shearing rate assuming negligible net ion flow shear ($V_E' + V_{di}' \approx 0$). Zero net flow shear is not supported by any data presented here but has frequently been employed in theoretical studies of the H-mode. The implications of this assumption will be examined in Sec. IV.

Furthermore, since T_i measurements were not available, $T_i \sim T_e$ has been employed. Unfortunately, a direct measurement of the shearing rate was not available, and no further use of V'_y will be made except for a few speculations related to Fig. 2. Here and throughout the paper the subscript notations x and y refer to the radial and (strictly speaking) binormal directions. In practice, the "y" direction is taken as approximately poloidal so that x and y lie in the gas puff imaging (GPI) viewing frame. See Refs. 10 and 11 for more details of the GPI diagnostic.

Note from Fig. 2 that radii in the range of −4 cm to −2 cm are close to the maximum characteristic frequencies for γ_{mhd} and ω_*. From Fig. 2 it can be seen that characteristic frequencies are much smaller in OH mode where gradients are smaller. In either of the operational modes, γ_{mhd} and ω_* are comparable; and in H mode our rough estimate of the shearing rate shows it to be much larger almost everywhere than γ_{mhd}, whereas in OH mode, the opposite is true. The zero in the shearing rate, corresponds to the location of the maximum pressure gradient under the assumptions previously discussed.

High quality turbulence data from GPI was available at −2 cm (as determined by the EFIT equilibrium reconstruction code) and data taken at this location is the basis for the remainder of the analysis in this paper. While −2 cm does not correspond to the precise maximum of the instability drive suggested by γ_{mhd} in Fig. 2, it is expected to be a relevant location for studying the scaling of turbulence characteristics. As described in Ref. 10, GPI data was analyzed by a correlation analysis and by blob tracking. For analyzing the turbulence drive region the correlation analysis was deemed

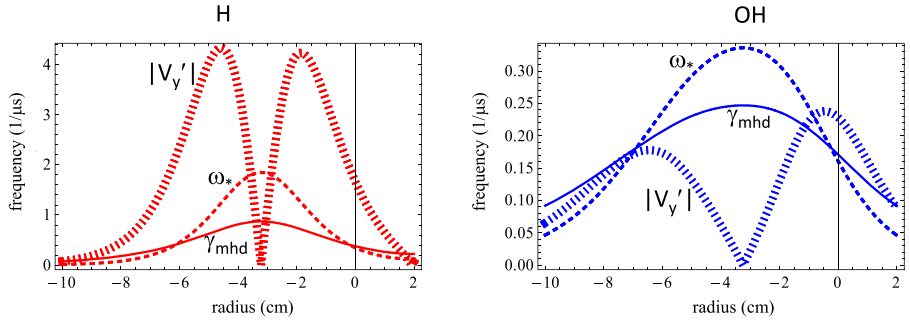

FIG. 2. Radial variation of several frequencies of interest for the subset database, H mode (left panel) and OH mode (right panel). Note the scale change in the vertical axis.

to be most relevant and this analysis method is used throughout the paper for the determination of characteristic turbulent spatial scales and velocities. In all of the scaling plots which follow, both the mean and standard deviation (resulting from the shot-to-shot variations) of the measured turbulence quantities for each operational mode are indicated, with the latter denoted by error bars. The specific quantities from the GPI database that enter the analysis that follows are: the radial and poloidal turbulence correlation lengths L_{rad} and L_{pol}, the radial turbulence velocity V_{rad}, the relative rms GPI fluctuation level $\delta I/I$, as well as the plasma profiles, their gradient scale lengths, and the local major radius and magnetic field at the outboard midplane.

III. SCALING BETWEEN OPERATIONAL MODES

In this section, the variation of length and time scales, and the role of resistivity between different operational modes is examined using both the large database and the subset database. For the large database, T_e measurements at -2 cm often had large estimated uncertainties and for some discharges no measurement was available. In other cases, uncertainties in profile gradient scale lengths and the occurrence of very small numbers in the denominators of the expressions being evaluated resulted in a small number of outliers that have been excluded from the analysis which follows.

The first quantity of interest is the length scale of the turbulence. This was also investigated in Fig. 8 of Ref. 10 but is repeated here for completeness. Figure 3 shows that, both radial and poloidal correlation lengths L_{rad} and L_{pol} scale almost linearly with ρ_s when the variation among operational modes is considered. A best fit yields $L_{rad} \sim L_{pol} \sim 17\ \rho_s$ where ρ_s is evaluated using the local magnetic field at the outboard midplane. This corresponds to $k_y\rho_s \sim 0.13$ where k_y is the binormal (approximately poloidal) wavenumber. It is estimated from the correlation length as $k_y = 2.1/L_{pol}$. (The factor of 2.1 comes from the particular definition of correlation length used in the database as applied to a sinusoidal waveform.) This result is consistent with drift waves or drift resistive modes as previously noted.[10]

Investigating the scaling of characteristic frequencies is more subtle. Autocorrelation times have already been reported;[10] however, they are not necessarily suitable for present purposes. As noted in Fig. 12 of Ref. 10, the autocorrelation time is likely dominated by convection, i.e., it is mainly determined by the flow velocities of the structures and their spatial size. Another estimate of the turbulence time scale in the plasma $E \times B$ drift frame is needed. We call this quantity ν_{turb} and use it as a proxy for the turbulence frequency in the drift frame, ω, in the scaling studies that follow. It is defined from the pressure continuity equation assuming that the time evolution is dominated by $E \times B$ convection

$$\nu_{turb}\tilde{p} \approx \tilde{v}_x p/\lambda_p. \tag{5}$$

In addition, we estimate $\tilde{p}/p \approx \tilde{I}/I$ where $\tilde{I}$ and I are the fluctuating and mean GPI emission intensities, respectively, and also we estimate $\tilde{v}_x \approx V_{rad}$ where V_{rad} is the radial turbulence velocity in the database obtained from a two-point time delay analysis. This time-delay analysis measures the average radial velocity of the fluctuations and would be zero if there were no fluctuations (i.e., only steady convection). The phase between $\tilde{p}$ and $\tilde{v}_x$ was not measured and is not important in our use of Eq. (5), but enters the evaluation of the turbulent flux and will be discussed in Sec. V.

Results for V_{rad} vs. $\lambda_p\tilde{I}/I$ are shown in Fig. 4; for any given mode of operation the slope $V_{rad}/(\lambda_p\tilde{I}/I)$ gives ν_{turb}. The data is scattered, but it will be seen subsequently that it becomes organized when ν_{turb} is plotted against other quantities. Thus, Eq. (5) is central to much of the subsequent analysis in this paper. For the full database we find an average $\nu_{turb} \sim 0.10\ \mu s^{-1}$ for OH and $0.17\ \mu s^{-1}$ for H mode; $0.06\ \mu s^{-1}$ for the OH7 subset, and $0.38\ \mu s^{-1}$ for the H7 subset. In order of magnitude $1/\nu_{turb}$ is similar to the autocorrelation time but there are significant differences when comparing operational modes. In Fig. 4 and all subsequent figures using the full database, λ_p is computed from the relation $\lambda_p = \lambda_n/2.6$, where the factor 2.6 is obtained from a fit using all the discharges. This procedure reduces the uncertainty in λ_p for a given

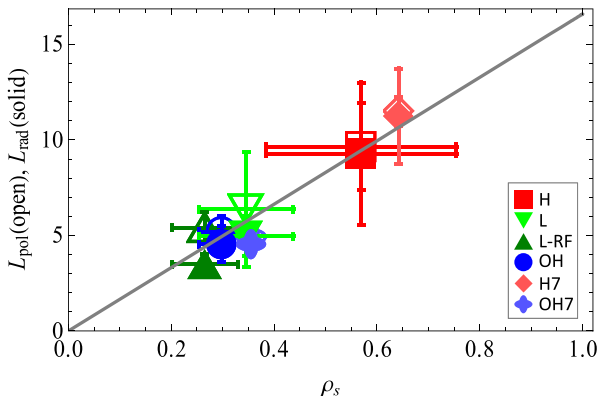

FIG. 3. Scaling of radial (solid symbols) and poloidal (open symbols) correlation lengths with the ion sound radius. The units of both axes are cm. Here and in subsequent figures, H7 and OH7 refer to the subset database. The gray line is a best fit constrained to pass through the origin.

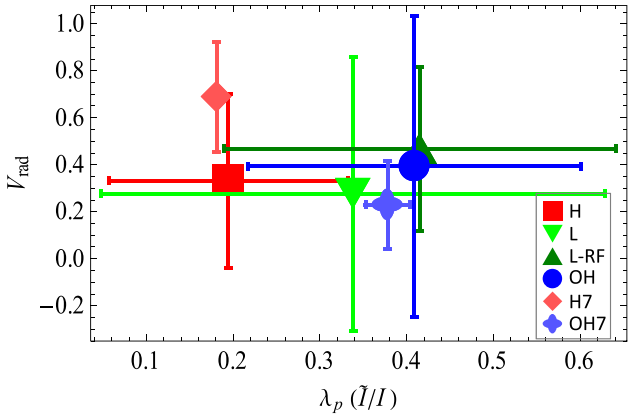

FIG. 4. Radial correlation velocity in km/s vs. relative fluctuation amplitude and pressure gradient scale length in cm. The individual slopes $V_{rad}/(\lambda_p\delta I/I)$ provide a measure of the turbulence rate ν_{turb}. Here and elsewhere in the figures $\delta I/I$ and the notation $\tilde{I}/I$ employed in the main text are synonymous.

discharge, since λ_n can generally be determined more accurately than λ_{Te}.

Using ν_{turb} it is now possible to compare the observed turbulence time scales with those expected for drift and curvature-driven modes. Figure 5 explores the drift character of the turbulence. Within error bars, $\nu_{turb} = 0.39\ \omega_*$ where ω_* is the drift frequency defined by Eq. (3) and k_y is again estimated as $k_y = 2.1/L_{pol}$. Although the error bars (standard deviations between discharges in a given mode) are large, the linear scaling is apparent and the ratio ν_{turb}/ω_* is order-of-magnitude as expected for drift physics. If $T_i \sim T_e$ then $|\omega_{*i}| \sim |\omega_{*e}|$ and drift dependence could indicate either electron drift wave physics or ion diamagnetic physics (such as might accompany interchange/ballooning modes). Note also from Fig. 3 that $k_y\rho_s$ is approximately a constant, so Fig. 5 also shows that $\nu_{turb} \propto c_s/\lambda_p$ similar to a result in Ref. 15.

As noted in Sec. II, the error bars in Figs. 3–8 indicate the standard deviation resulting from the shot-to-shot variations of the measured quantities for each operational mode. The uncertainty in the estimate of the mean for each operation mode (assuming statistical independence of the values in the sample) is smaller by $1/N^{1/2}$ where the number of samples N is 93 for H mode and 33 for OH, 9 for L mode and 5 for L-RF mode. This may be a more relevant estimate of actual uncertainties for our present goal of exploring the scaling of the turbulence *between* the different operational modes (as opposed to looking for scaling among the cluster of data points within a given operation mode).

The turbulence also displays a frequency scaling that is suggestive of curvature-driven interchange or ballooning modes. A characteristic interchange or magneto-hydrodynamic (MHD) growth rate is given by Eq. (2). Within error bars, one obtains $\nu_{turb} = 0.6\ \gamma_{mhd}$. Both the linear scaling and the order-of-magnitude suggest that curvature-driven physics is at work. The fact that ν_{turb} lies somewhat below γ_{mhd} is not surprising: many effects suppress ideal MHD growth below the estimate of Eq. (2) such as magnetic shear, ion diamagnetic physics, and the variation of curvature along the magnetic field.

Figures 5 and 6 make a case for drift-interchange turbulence, which is strengthened if the error bars are additionally reduced by $1/N^{1/2}$ due to sample size, and becomes most compelling when the fits are constrained to pass through the origin, as expected theoretically. It will be noted from Eqs. (2) and (3) that $\gamma_{mhd} \propto (T_e/\lambda_p)^{1/2}$ whereas $\omega_* \propto (k_y\rho_s)\ T_e^{1/2}/\lambda_p \propto T_e^{1/2}/\lambda_p$ (given that from Fig. 3, $k_y\rho_s$ is nearly constant). Thus, γ_{mhd} and ω_* are strongly correlated and this is evident from the parameters on the horizontal axis of Figs. 5 and 6. Perhaps more important than their scaling is the fact that γ_{mhd} and ω_* are numerically within a factor of two of each other for each of the operational modes. This is evidence that interchange and drift physics are both important. Evidently, the plasma has selected profiles and turbulent k_y values to make this occur.

In this database, the parameter $\nu_{e*} = \nu_{ei}R/v_{te}$ (where ν_{ei} is the electron-ion collision frequency and v_{te} is the electron thermal velocity) at the outboard midplane ranges between 1 and 5 for OH, L and L-RF cases and between 0.1 and 1 for the H mode cases, suggesting a role for collisionality in the former. To explore this possibility, it is interesting to examine the data in terms of a parameter relevant to resistive ballooning. In resistive ballooning theory there is a competition between the stabilizing effect of magnetic line bending and resistive diffusion of the magnetic field which relaxes the "frozen-in" condition on the time-scale of the wave

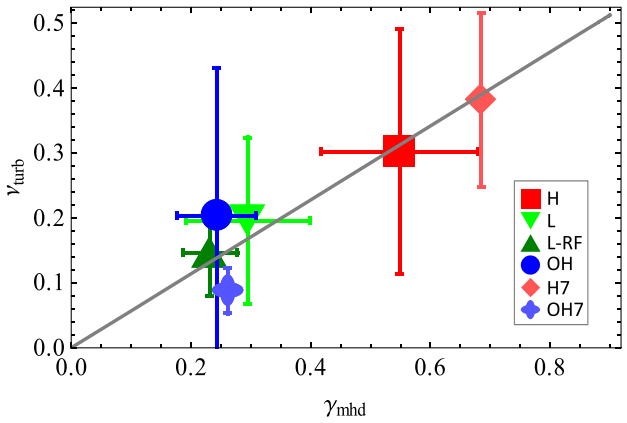

FIG. 6. Curvature-driven interchange character of the turbulence. Turbulence and drift frequencies are given in μs^{-1} and the gray line is a best fit constrained to pass through the origin.

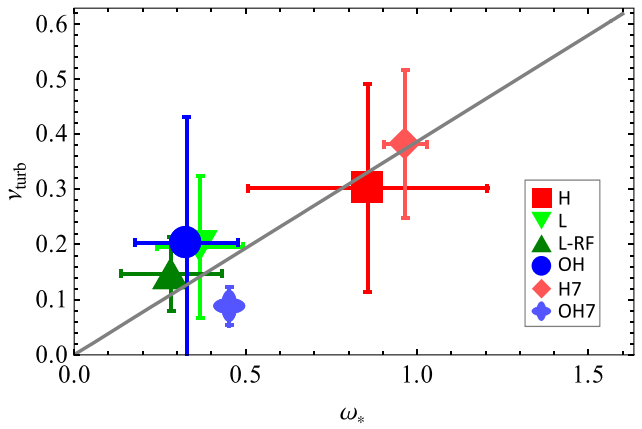

FIG. 5. Drift character of the turbulence. Here the turbulence and drift frequencies are given in μs^{-1}. The gray line is a best fit constrained to pass through the origin.

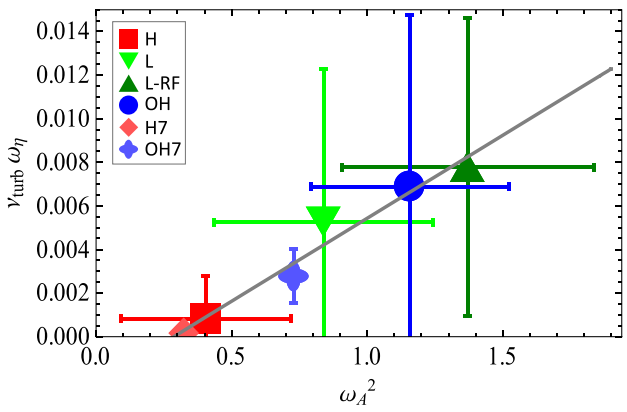

FIG. 7. Role of resistive ballooning physics. Turbulence and drift frequencies are given in μs^{-1} and the gray line is an unconstrained best fit. Here ω_η is calculated using outer-midplane values.

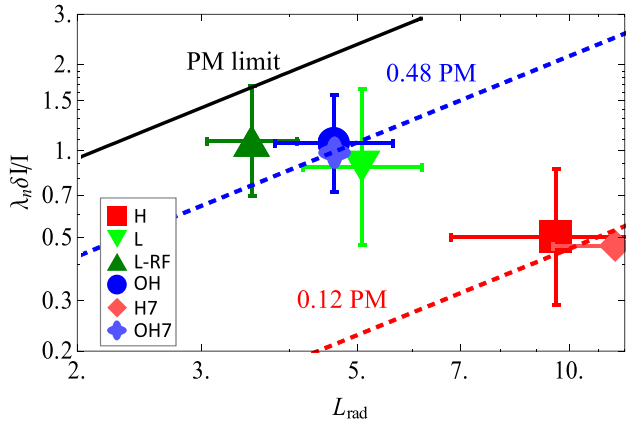

FIG. 8. Saturation level diagram showing each operational mode relative to the profile-modification (PM) limit. In this plot, the PM limit (solid black) and fractions thereof (0.48 dashed blue; 0.12 dashed red) are represented by diagonal lines. The chosen plotted lines are for reference to the location of the two groupings ([OH, OH7, L, L-RF] and [H, H7]). Units for both axes are cm.

(instability). The fastest growing resistive ballooning instabilities typically balance the two competing effects resulting in

$$\omega\omega_\eta \sim \omega_A^2, \tag{6}$$

where $\omega_\eta = k_\perp^2 \delta_e^2 \nu_{ei}$ is the magnetic diffusion rate, $\delta_e = c/\omega_{pe}$ is the electron skin depth, $\omega_A = v_A/R$ is the Alfvén frequency, and $v_A = B/(4\pi n_i m_i)^{1/2}$ is the Alfvén velocity. (See for example, Eq. (8) of Ref. 27 and references therein.) Results for the comparison of Eq. (6) with data are shown in Fig. 7 where again ω is estimated as ν_{turb}. For the estimate of ω_η we have used the collisionality and wavevector at the outboard midplane, with $k_\perp \sim k_y \sim 2.1/L_{pol}$.

From the vastly different scales of the two axes in Fig. 7 it is clear that $\omega\omega_\eta$ and ω_A^2 are not comparable at the outer midplane where ω_η has been estimated; at that location $\omega\omega_\eta/\omega_A^2 \ll 1$ and hence resistive effects are negligible. Nevertheless, the linear correlation displayed in the plot suggests a role for resistive effects. A candidate explanation is resistive X-point physics[32,33] for the OH, L, and L-RF cases. The magnetic geometry of the X-point region enhances the role of resistivity for several reasons. In some discharges the collisionality itself may be somewhat higher in the X-point region due to neutral recycling at the divertor which increases the local density and lowers the temperature. Independent of this possibility, local magnetic shear in the X-point causes a large enhancement of $k_\perp$ when filamentary (field aligned blob) structures are mapped from the outboard midplane to the X-point region.[34,35] The net effect is that ω_η grows rapidly near the X-points; modes which are ideal interchange-like in the midplane become resistive close to the X-points resulting in an eigenfunction that can localize to the bad curvature region without paying much of a stabilizing line-bending penalty.[32] The three dimensional structure and dynamics of fluctuations near the separatrix is an active area of experimental investigation; there is some good evidence for correlation of midplane and divertor regions in the SOL,[36,37] and shear-induced disconnection near the separatrix.[36]

From Fig. 7, estimating from the linear fit at $\omega_A = 1$, an X-point enhancement of ω_η of about 180 would be required to satisfy Eq. (6). Making the conservative assumption that ν_{ei} is constant along a flux surface, a required X-point enhancement of $k_\perp$ of about 14 would be needed. This magnitude of enhancement factor is well within a typical calculated range. (See for example, Fig. 1 of Ref. 32 which shows ω_η varying by more than two orders of magnitude.)

The tentative conclusion is that resistive X-point physics is likely at work for these OH, L, and L-RF cases and could easily result in an associated type of resistive ballooning mode that is not inconsistent with the experimental data. This conclusion is consistent with work by other authors. For example, the importance of resistive ballooning physics for an L mode discharge in the DIII-D tokamak was shown in three-dimensional fluid simulations that included the X-point geometry explicitly.[20] For the H mode cases, resistivity does not appear to be important, but this hardly affects the character of the modes at the outboard midplane.

IV. SATURATION PHYSICS

The saturation levels of the turbulence in the steep gradient region just inside the separatrix are also of great interest, in order to understand turbulent transport into the SOL heat exhaust channel (i.e., the near SOL) and also into the far SOL. It is in this steep gradient region near the separatrix where coherent blob structures are thought to be born, and where their outward convective transport begins.[3,4]

Figure 8 shows the saturation levels in a parameter space that allows comparison to a simple profile-modification (PM) estimate. The PM estimate, sometimes called a mixing length estimate, equates the perturbed and equilibrium gradients

$$k_x \tilde{n} = n/\lambda_n, \tag{7}$$

where we take $k_x = 2.1/L_{rad}$ and $\tilde{n}/n = \tilde{I}/I$. This figure recapitulates similar information from Ref. 10. As noted there, the OH and L mode saturation levels are close to, but somewhat below, the PM estimate; the H-mode levels are well below. Arguably, for pressure gradient rather than density gradient driven modes, one should use λ_p instead of λ_n in Eq. (7), in which case, the proximity of the PM estimate for the (OH, OH7, L, L-RF) group is a little less convincing, falling to 0.18 PM instead of 0.48 PM. H-mode levels are in any case well below the PM level at 0.12 or (with λ_p instead of λ_n) 0.046. Note also that in the pressure gradient driven case, the wave-breaking saturation estimate given by $k_x \tilde{v}_x = \nu_{turb}$ with the definition of ν_{turb} given in Eq. (5) is equivalent to the PM estimate.

In some cases, particularly for H-mode plasmas, it has been suggested[16,19,27] that large scale convective eddies of turbulence generated in the lower pedestal gradient region carry plasma across the separatrix, and therefore, provide the turbulent cross-field flux that competes with parallel losses to set the SOL width. In these cases, it is argued that λ_q in the SOL varies inversely with λ_p in the lower pedestal. An estimate of λ_p in the lower pedestal is, therefore, of interest and may be obtained by balancing the diamagnetic and

$E \times B$ drifts (giving $\lambda_p \sim \lambda_E$). Employing Eq. (4) and equating the shearing rate V'_y to γ_{mhd} yields the order of magnitude estimate[27]

$$\lambda_p \sim R^{1/3} \rho_s^{2/3}. \quad (8)$$

This condition is conceptually the one for turbulence suppression by $E \times B$ shearing, which is commonly thought to be active in H-mode plasmas.

A scatter plot of individual discharges in the plane of a parameter $C_\lambda \equiv \lambda_p/(R^{1/3}\rho_s^{2/3})$ and fluctuation amplitude is shown in Fig. 9. Most H modes are seen to lie in the lower left quadrant, and most OH, L, and L-RF modes lie in the upper right quadrant. The demarcation of the quadrants does not occur exactly at $C_\lambda = 1$; however, given the heuristic nature of Eq. (8), this is not surprising. A few "anomalous" points lie outside of the expected quadrants. The analysis comes with significant caveats: λ_{pe} is used as the pressure gradient scale length in the plot, but really λ_{pi} should be used for the ion diamagnetic drift, and the total species summed λ_p should be used in estimating γ_{mhd}. Nevertheless a qualitative trend is apparent. It can be verified (not shown here) that $C_\lambda < 1$ is characteristic of the smoothed H7-mode profiles of Fig. 1 from −4 cm on out to beyond the separatrix.

Figure 9 shows directly that C_λ roughly characterizes the different operational mode groups with small C_λ corresponding to H modes. Since H modes have steeper gradients, this is not surprising. However, assuming $\lambda_p \sim \lambda_E$ it follows that $C_\lambda \approx (\gamma_{mhd}/V_y')^{2/3}$. Thus C_λ being of order unity is suggestive that interchange and $E \times B$ shearing rates are somewhat comparable for all of these NSTX plasmas, and that $E \times B$ shearing becomes relatively stronger for H modes.

Following Ref. 5, the present data may also be plotted in the space of $\alpha_{mhd} \sim \gamma_{mhd}^2/\omega_A^2$ and $\alpha_d \sim \omega_{*i}/\gamma_{mhd}$. The ratio α_{mhd} represents the competition in ideal magnetohydrodynamics (MHD) between the interchange free energy driving instability, γ_{mhd}, and the stabilizing effect of magnetic field line bending, ω_A. The ratio α_d is a measure of the importance of ion diamagnetic drift effects in stabilizing the ideal MHD interchange instability. We choose not to present this type of plot here because of ambiguities in how to evaluate α_{mhd} in these strongly shaped spherical torus plasmas, whereas the original work[5] was developed for a circular flux surface model. Furthermore, the ω_{*i} in the definition of α_d in the theory[5] should be calculated using the characteristic wavenumber given by Eq. (6) using $\omega \sim \gamma_{mhd}$. As already pointed out in connection with Fig. 7, this wavenumber is much larger than the measured $k_y \sim 2.1/L_{pol}$ at the outboard midplane. Again, the difference could be reconciled by invoking X-point magnetic shear. Qualitatively, we can say, that the H-mode cases have larger values of α_{mhd} and α_d relative to the OH and L mode cases, as expected from the model of Ref. 5.

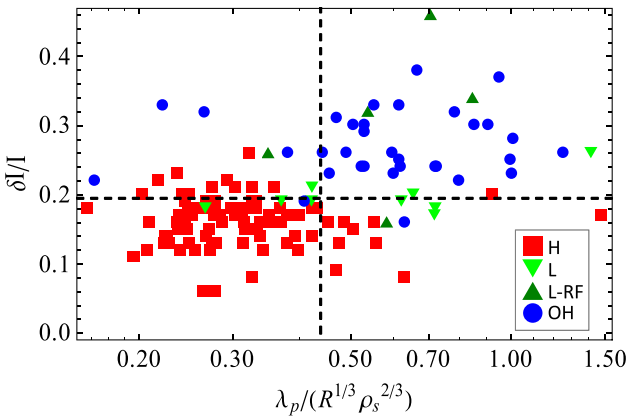

FIG. 9. Regime diagram for turbulence suppression by ion pressure gradient induced $E \times B$ shearing. The dashed lines are a guide to the eye. Their location was determined to show roughly the same number of "anomalous" points on each side of the line.

V. DISCUSSION AND IMPLICATIONS FOR THE SOL WIDTH

Before proceeding with more speculative applications of the scalings determined in Sec. III, it is instructive to estimate λ_q from Eq. (1) in the most direct way possible. The idea here is that turbulence generated in the region where the measurements were taken, just inside the separatrix, is responsible for the turbulent transport into the SOL. For this purpose we let $\langle \tilde{p}\, \tilde{v}_x \rangle \approx |\tilde{p}|\,|\tilde{v}_x|$ ignoring a possible cross-phase which would reduce the estimate. (We know that $\tilde{p}$ and $\tilde{v}_x$ are at least somewhat correlated and in phase, as most detected blobs move outward as expected from their interchange character.) For the data employed here $\tilde{p}/p \sim \delta I/I \sim 0.16$ and 0.27 in H and OH modes, respectively. Also $\tilde{v}_x/c_s \sim V_{rad}/c_s \sim 0.007$ and 0.018 in H and OH modes, respectively. This gives a direct estimate of $q_\perp/(pc_s) \sim 1.1 \times 10^{-3}$ and 4.9×10^{-3} in H and OH modes, respectively. For the parallel factor qR/g we use $qR \sim q_{95}R_0$ where $R_0 \sim 85$ cm and q_{95} ranges from 6 to 14 in the database. A rough estimate is $qR \sim 800$ cm which is also comparable to the connection length in the SOL. For the parallel energy transmission factor we invoke the sheath limited regime with sheath energy transmission factor $g \sim 5$. These rough estimates result in a midplane SOL heat flux width due to turbulence of $\lambda_q \sim 0.2$ cm in H mode and 0.8 cm in OH mode, similar in order of magnitude to previous estimates made for the subset database using a somewhat different method.[11] Typical H mode inter-ELM midplane-mapped heat flux widths measured in NSTX are in the range of 0.2 to 1.5 cm (without Li injection) depending on I_p, the plasma current.[38] At the highest plasma currents the midplane width, correcting for diffusive broadening in the divertor legs, is $\lambda_q \sim 0.2$ cm, comparable to the turbulence estimate deduced here. The experimentally observed scaling[28] of λ_q in this and other devices (for H mode diverted discharges) is well described as having an inverse dependence on I_p suggestive of neoclassical drift-orbit physics[39] but it would be significant if turbulence led to different scaling effects at large I_p.

Since turbulence may reasonably be argued as relevant for setting λ_q, though perhaps subdominant in present devices, it is interesting to investigate the implications for scaling under the plausible assumption that the drift-interchange character of edge turbulence found here is universal. Recalling Eq. (1) and invoking the definition of ν_{turb} in

Eq. (5) and neglecting the $(\tilde{p}, \tilde{v}_x)$ cross-phase, one obtains the order-of-magnitude estimate

$$\lambda_q \approx \frac{qR}{g}\frac{\tilde{p}^2}{p^2}\frac{\lambda_p \nu_{turb}}{c_s}. \tag{9}$$

A dimensionless saturation amplitude f_{pm} may be defined relative to the pressure profile modification limit as

$$\frac{\tilde{p}}{p} = \frac{f_{pm}}{k_x \lambda_p} \tag{10}$$

which allows λ_q to be written as

$$\lambda_q = \frac{qR}{g}\frac{f_{pm}^2 \nu_{turb}}{k_x^2 \lambda_p c_s}. \tag{11}$$

At this point, the scaling of ν_{turb} can be invoked. From the analysis of the drift-wave character in Fig. 5 we have

$$\nu_{turb} = C_{dw}\omega_* = \frac{C_{dw} k_y c_s \rho_s}{\lambda_p}, \tag{12}$$

where C_{dw} is an order unity dimensionless number determined to be ~0.39 from this dataset. On the other hand, from the analysis of the curvature-interchange character in Fig. 6 we have

$$\nu_{turb} = C_{mhd}\gamma_{mhd} = \frac{C_{mhd} c_s}{(R\lambda_p)^{1/2}}, \tag{13}$$

where C_{mhd} is another order unity dimensionless number ~0.6 for this dataset. Equating the two expressions for ν_{turb} yields

$$\frac{\lambda_p}{R} = \frac{C_{dw}^2 C_{k\rho}^2}{C_{mhd}^2}, \tag{14}$$

where $C_{k\rho} \equiv k_y \rho_s$ is a third dimensionless number which is ~0.13 for this dataset (and typical for drift waves in a variety of contexts). Equations (11), (14) and either of (12) or (13) may be combined to eliminate ν_{turb} and λ_p resulting in

$$\lambda_q = \frac{qR}{g}\frac{f_{pm}^2 C_{mhd}^4 \rho_s^2}{C_{dw}^3 C_{k\rho}^5 R^2}. \tag{15}$$

Here, the assumption $k_x \approx k_y$ has been used, which is justified by Fig. 6(c) in Ref. 10 which shows that the correlation lengths L_{rad} and L_{pol} are comparable at a radius of −2 cm.

This is as far as the assumption of drift-interchange turbulence alone can take us. The explicit scaling (in particular, neglecting any implicit scaling in f_{pm}) is $\lambda_q \propto q\ \rho_s^2/R$ while the neoclassical drift-orbit scaling[39] is $\lambda_q \approx q\rho_s$. They share a common factor of $q\rho_s$ and their relative size will depend on the product of ρ_s/R and a potentially large pre-multiplier.

Making a plausible additional assumption allows further reduction of Eq. (15). Motivated by Eq. (8) we employ the dimensionless number $C_\lambda \approx (\gamma_{mhd}/V'_y)^{2/3}$ given by the relation

$$\lambda_p = C_\lambda R^{1/3}\rho_s^{2/3}. \tag{16}$$

From Fig. 9 (an average over the data therein) we find $C_\lambda \sim 0.33 \pm 0.16$ for H mode and $\sim 0.63 \pm 0.24$ for OH modes. (C_λ for L and L-RF are similar to OH. Alternatively using the subset database, $C_\lambda \sim 0.26$ for H mode and ~0.44 for OH.) Then, combining Eqs. (14) and (16) yields

$$\frac{\rho_s}{R} = \frac{C_{dw}^3 C_{k\rho}^3}{C_{mhd}^3 C_\lambda^{3/2}} \tag{17}$$

and Eq. (15) can be expressed in the form

$$\lambda_q = \frac{qR}{g}\left(\frac{f_{pm}^2 C_{dw}^3 C_{k\rho}}{C_{mhd}^2 C_\lambda^3}\right) \approx \frac{qR}{g}\frac{f_{pm}^2}{51\ C_\lambda^3}. \tag{18}$$

The derivation of Eq. (18) is clearly heuristic, and rests on several assumptions. It is meant as a physics-based framework from which to approach future work in assessing turbulence effects on the SOL width. This form expresses the normalized perpendicular heat flux $q_\perp/(pc_s)$, i.e., the expression in parenthesis in Eq. (18), entirely in terms of (nominally order unity) dimensionless numbers that are physically based on the characteristics of the turbulence. The final form of Eq. (18) uses the values of $C_{dw} = 0.39$, $C_{mhd} = 0.6$ and $C_{k\rho} = 0.13$ deduced from the database; for drift-interchange turbulence they might be almost universal numbers which should not influence the overall scaling. The most uncertain, or highly variable, of the inputs are the saturation level f_{pm} and the value of C_λ, which unfortunately appear with rather high powers. Of course when the appropriate f_{pm} and C_λ are used, Eq. (18) gives similar numerical values for $q_\perp/(pc_s)$ and λ_q in H and OH modes as the direct estimate given in the first paragraph of this section. However, the present form may be useful as a physics-based technique for extrapolating to other situations and devices, provided the underlying assumptions hold there as well.

It is interesting to compare the present scaling with that of the experimental multi-machine database[28] for diverted H mode discharges. The two scalings are not the same. The interesting possibility is that the physical mechanisms underlying the present multi-machine database may not be turbulent and may not hold for larger machines. The multi-machine database scaling is nearly independent of R and gives roughly $\lambda_q \sim q\rho_s \propto 1/I_p$ suggestive of a drift-orbit[24,39] (i.e., non-turbulent) mechanism.

In contrast, the only explicit scaling remaining in Eq. (18) is $\lambda_q \propto qR \propto \varepsilon^2 R^2 B/I_p$ where $\varepsilon = a/R$. Like the multi-machine experimental scaling[28] and the heuristic drift-orbit scaling[39] Eq. (18) has an inverse dependence on Ip. This fact may make it difficult to distinguish between mechanisms based on scaling results alone. Unlike the multi-machine and the heuristic drift-orbit scalings, however, Eq. (18) has an explicit increase with R. Thus the turbulence mechanism could become dominant for large devices, especially at large plasma current I_p where the $q\rho_s$ scaling would predict extremely small λ_q. The fact that the experimental multi-machine scalings for diverted H mode[28] and limited L

mode[29] discharges are different suggests a role for competing mechanisms.

Finally, we can speculate on the generality of the present results for f_{pm} and C_λ. The physics behind Eq. (16) is that ion-pressure-gradient-induced $E \times B$ shearing is suppressing curvature-driven interchange-ballooning modes. This may be reasonable for H modes and should result in an order unity, roughly constant, value for C_λ. The same argument cannot readily be made in general for OH or L modes; so it is indeed possible that C_λ contains additional scaling, or that Eq. (16) ceases to be useful, in those operational modes.

Concerning saturation levels, especially for H modes, the f_{pm} factor becomes rather small according to Fig. 8 and it is far from certain that the profile modification or wave breaking condition is a relevant quantity with which to normalize the residual turbulence in H mode plasmas. One speculative possibility is that when interchange-ballooning modes are suppressed by $E \times B$ flow shear with $V_y' \sim \gamma_{mhd}$ then the system becomes unstable to secondary Kelvin Helmholtz (KH) instability.[40,41] KH growth rates are known to be at most $\gamma_{kh} \sim 0.2\ V_y'$ (see for example, Ref. 42 and contained references in the introduction) and the wave breaking condition for them, $k_x\ \tilde{v}_x \sim \gamma_{kh}$, would be correspondingly smaller than the wave breaking condition for the primary γ_{mhd} instability. Further investigation of this point is warranted.

VI. REDUCED MODEL SIMULATIONS

Numerical simulation provides a means to test the role of drift-interchange physics, sheared flows, and turbulence levels on the SOL heat flux width. Ultimately, the generality of the scaling approach discussed in Sec. V could be tested and values determined for the five dimensionless parameters: the drift-interchange parameters C_{dw}, C_{mhd}, and $C_{k\rho}$, the sheared flow parameter C_λ and the saturation level parameter f_{pm}. In this section, we report on some results using the SOLT code, which incorporates a reduced 2D fluid turbulence model for the edge and SOL. The basic model, described in detail in Ref. 19, incorporates fluid evolution equations for the advection of density, electron and ion temperatures and a generalized vorticity from which the electrostatic potential is extracted. The simulation plane is the 2D plane perpendicular to the magnetic field at the outboard midplane. Analytical closures are employed to describe parallel physics such as end losses in the SOL.

Previous studies of the SOL width with the SOLT code have confirmed the scaling remaining in Eq. (18) from the SOL connection length $L_{||} \sim qR$. The $L_{||}$ dependence has a simple explanation in terms of the parallel confinement time. This dependence was explored in Ref. 43 where SOLT results showed an increase of λ_q with $L_{||}$. The scaling was consistent with diffusive cross-field transport $\sim L_{||}^{1/2}$ in the weak turbulence regime, and transitioned to a scaling similar to $L_{||}$ in the regime of stronger blob-dominated turbulent convection. In the following we explore the scaling with fluctuation amplitude for a particular discharge, and examine the dimensionless parameters in Eq. (18) that characterize the turbulence.

Simulations were carried out for NSTX H-mode discharge #127975 (plasma current $I_p = 1$ MA, neutral beam power $P_{NBI} = 6$ MW, and magnetic field $B_t = 0.4$ T). The use of the SOLT code in this application is best described as interpretive: particle and heat sources, the separatrix location R_{sep}, and diffusion coefficients were varied to obtain a best fit match to the measured density and temperature profiles, the power flowing in the SOL P_{sol}, and the fluctuation level at the separatrix $(\delta n/n)_{sep}$. (Small changes, within magnetic reconstruction uncertainties, in R_{sep} with respect to the profiles measured by Thomson scattering, $n_e(R)$ and $T_e(R)$ have a significant effect on P_{sol} requiring the variation of R_{sep} as a parameter.) In addition to turbulence which causes transport through both turbulent convection and diffusion, SOLT allows additional explicit diffusion coefficients in the evolution equation for n_e, T_e, T_i, and vorticity, viz. (D_n, D_{Te}, D_{Ti}, D_ρ). These describe diffusive transport processes outside the scope of the SOLT model, e.g., neoclassical transport, transport processes due to neutral charge-exchange, and instabilities that are not explicitly modeled.[19] Our best simulation case achieves good profile matching to Thomson scattering measurements and turbulence values comparable to typical H-modes in the database: viz., SOLT finds $k_y\rho_s = 0.17$, $P_{sol} = 5.4$ MW with intermittent variations up to 6.1 MW, and $(\delta n/n)_{sep} = 0.22$ decaying rapidly into the closed surface region. The corresponding explicit diffusivities for this case are $(D_n, D_{Te}, D_{Ti}, D_\rho) = (0.04, 0.04, 0.2, 0.2)\ c_{sr}\rho_{sr}$ where the reference normalization has the value $c_{sr}\rho_{sr} = 147\ m^2/s$ for this simulation. It will be noted that D_{Ti} and D_ρ are quite large and imply explicit ion diffusive fluxes which are comparable to the turbulence-induced fluxes.

From this base case the turbulent dissipation was varied as a control parameter for $(\delta n/n)_{sep}$ to test the effect of turbulence on λ_q. Motivated by previous studies,[19] the turbulent dissipation parameter was taken as the density diffusion coefficient D_n which here was also held equal to D_{Te}. It was found that increasing D_n and D_{Te} *decreased* both the fluctuation levels and the resulting λ_q. Consequently, D_n and D_{Te} were primarily damping fluctuations which affect λ_q, not driving λ_q directly (in which case λ_q would have *increased* with D_n and D_{Te}). Results from the D_n scan are shown in Fig. 10.

Although explicit diffusion from D_{Ti} and D_ρ is responsible for contributing to λ_q in this simulation, Fig. 10 shows that turbulence has an order unity effect on λ_q which increases with the turbulence level. For this discharge the measured heat flux width at the divertor target (using the Eich[28] S and $\lambda_{q,t}$ fit parameters) is $\lambda_{q,t} = 5.2$ cm.[44] This implies a mid-plane-mapped λ_q of 0.4 cm which is a bit larger than, but comparable to, the SOLT simulation results in Fig. 10. For comparison, relative fluctuation levels for typical H-mode discharges are in the range 0.10 to 0.25. The simulations, therefore, suggest that the effect of turbulence is neither dominant or negligible for this $I_p = 1$ MA discharge. It is possible that other physics, such as neoclassical drift effects,[39] could explain the main $\lambda_q \sim 1/I_p$ scaling that is observed in NSTX[38] but that turbulence is still important, emerging as dominant only at larger I_p (or in larger R devices).

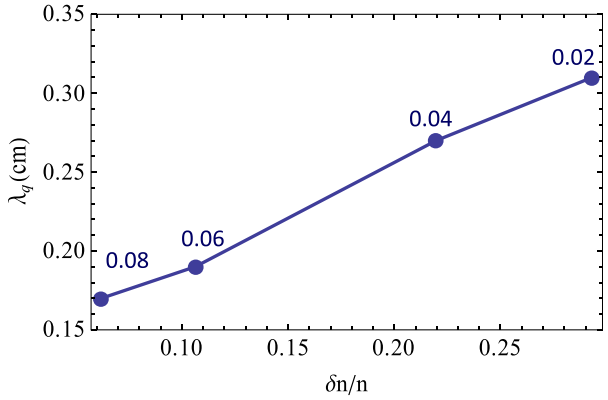

FIG. 10. Heat flux widths λ_q from a simulation scan in which D_n and D_{Te} were varied to control the fluctuation level at the separatrix $\delta n/n$. The values of the diffusion coefficient, in Bohm units, are indicated beside each simulation point.

Figure 11 shows a snapshot of the simulated density in the RZ plane. From panel (a) where $\delta n/n$ is displayed, blob structures are visible only in the SOL, with the most prominent structures in the region 2 to 4 cm beyond the separatrix. These density structures are accompanied by dipolar structures in the fluctuating potential, illustrated by the superimposed gray contours. The appearance of blobs mainly in the SOL for H mode discharges is a common feature of the GPI observations, as noted in Ref. 11. Panel (b) displays the total density in a radially stretched view. Turbulent transport that contributes to λ_q is not primarily resulting from discrete blobs, which have not yet fully formed at this location, but is rather due to wavy density structures that convect plasma back and forth across the separatrix. These are similar to the separatrix spanning convective cells noted in earlier SOLT simulations of another discharge.[16]

In addition to the large scale drift turbulence and blob features in Fig. 11, some fine scale striations can be seen near the separatrix. These NSTX spherical-torus H-mode plasmas have very sharp edge gradients with strong shear in the ion diamagnetic and E × B flows. The approximately stationary, strongly sheared flows tend to evolve fluctuations with moderate k_y to arbitrarily large k_x (by "stretching"), resulting in the striations. Diffusion coefficients large enough to suppress the formation of the striations are inconsistent with those determined to be appropriate for the experiments considered here. These features are the subject of ongoing studies.

This best case SOLT simulation is a first step in connecting the modeling of edge turbulence to the properties deduced from GPI in Secs. III and IV and to their implications for turbulence-based SOL width scaling in Sec. V. First, recall that the SOLT model is specifically constructed to describe drift-interchange turbulence, which is the type of turbulence deduced from the experimental data. Furthermore, drift-resistive ballooning modes have a drift-interchange character at the outboard midplane where the SOLT model is applied. Next, from Sec. V, recall that the most important characteristics of the turbulence are: the normalized saturation level (f_{pm}), the ω_* and γ_{mhd} dependence of ν_{turb} (described by C_{dw} and C_{mhd}), the $k\rho$ scaling ($C_{k\rho}$), and the sheared flow postulate (described by C_λ).

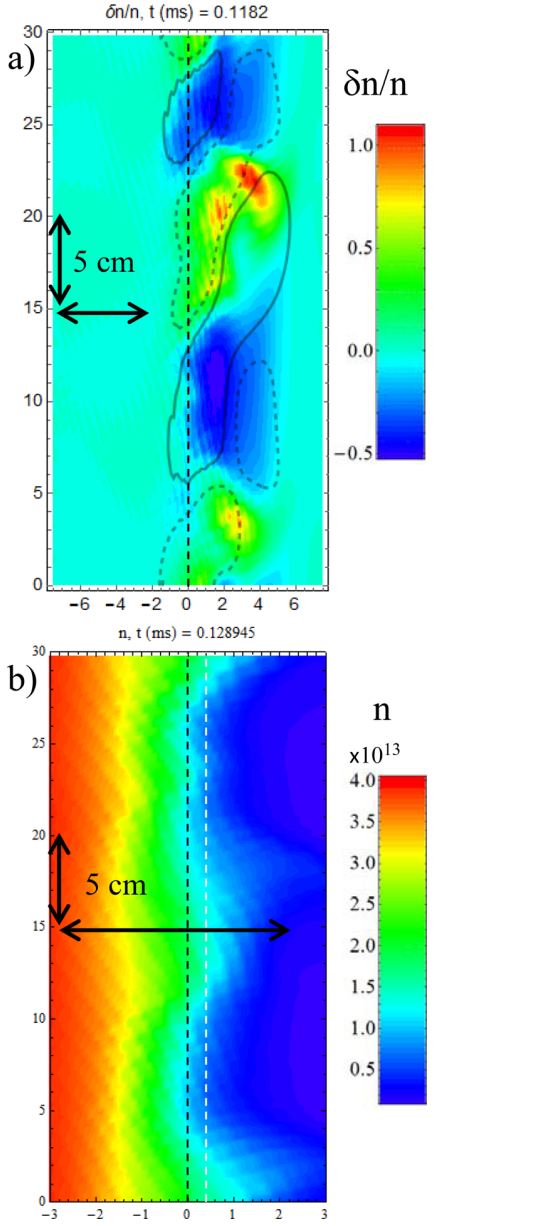

FIG. 11. Snapshot of the simulated density in the R (horizontal) and Z (vertical) plane. Part a) shows the relative density fluctuation $\delta n/n$ (where n in the denominator is the Z-averaged value at each R). The dashed black line is the separatrix. The superimposed gray lines show smoothed ±25 eV potential fluctuation contours (solid for positive, dashed for negative). Part b) shows the density itself, in a view which stretches the R coordinate to make features on the scale of λ_q visible. For reference, the dashed white line is located at $\lambda_q = 0.4$ cm. The fine scale striations in these figures are related to the strongly sheared flows (see text).

The present interpretive simulation is constructed to match the experimental plasma profiles and saturation level; therefore, C_λ and f_{pm} are inputs to the model. However, $C_{k\rho}$, C_{dw}, and C_{mhd} can be compared with the values deduced in Sec. III. The simulation gives $C_{k\rho} \sim 0.17$, which is close to the database value 0.13 deduced from Fig. 3. Simulation results for C_{dw} and C_{mhd} at the separatrix are approximately 0.1 and 0.3, respectively, which are factors of 2 to 4 smaller than the mean database values. However, in obtaining these

values a different procedure for estimating δv_x in the definition of ν_{turb} in Eq. (5) was employed for the simulations and the experimental data. The simulation analysis used the estimate $\delta v_x = \Gamma/n$ where Γ is the average radial particle flux, whereas the database analysis used a time delay correlation estimation (TDE) method to obtain the mean radial velocity of the turbulence. The different treatment is because the TDE method applied to the simulation was inconclusive: meaningful results could not be obtained, possibly due to the presence in the simulation of some blob structures with very rapid poloidal motion. Finally, and possibility related, the simulations exhibit strong $E \times B$ flow shear and it is likely that Kelvin-Helmholtz modes are playing a role in the saturated turbulent state. It will be important to determine if this remains the case in more complete turbulence models.

Additionally, while γ_{mhd}, ω_* and V'_y should still provide important characteristic frequencies in future larger devices with lower collisionality, kinetic simulations[25] would likely be needed to accurately study the turbulent physics.

VII. SUMMARY AND CONCLUSIONS

While there is considerable shot-to-shot variation of turbulence quantities such as fluctuation amplitudes, radial and poloidal correlation lengths, and radial and poloidal turbulence velocities within a given operational mode in NSTX, and even with in a given discharge, some interesting scalings emerge when considering the mean values of these quantities and their variation among operational modes. In this paper, we have considered Ohmic (OH), low (L), low with applied rf (L-RF), and high (H) mode plasmas from a large NSTX database, together with a seven-member subset database of OH and H mode discharges (denoted OH7 and H7). The length and time scales of the turbulence are found to be consistent (or more conservatively stated, not inconsistent) with drift-resistive ballooning modes, driven at least in part by curvature, and possibly affected by sheared flows. The characteristics of the turbulence are summarized as follows: $k_y\rho_s \sim 0.13$ where k_y is the binormal (approximately poloidal) wavenumber and ρ_s is evaluated using the local outboard midplane magnetic field; ω in the drift frame, estimated by ν_{turb} roughly scales like $\omega \sim 0.4\ \omega_* \sim 0.6\ \gamma_{mhd}$. These conclusions are made possible by the use of a proxy for the local wave frequency in the plasma frame given by Eq. (5), which is central to this paper. An argument was made in favor of resistive X-point effects likely being at work for OH and L modes. Turbulent fluctuation levels are much closer to the wave breaking or profile modification limits for OH and L modes, than for H modes which are well below those levels. H modes roughly occupy a parameter regime where $\lambda_p/(R^{1/3}\rho_s^{2/3}) < 0.4$ as might be expected if ion-pressure-gradient-induced $E \times B$ shearing is suppressing curvature-driven interchange-ballooning modes.

These results, all taken just inside the separatrix (2 cm inside the nominal EFIT separatrix) may be useful in guiding the ongoing work on the effect of turbulence in controlling the SOL heat flux width. Generally the apparent character of the modes is consistent with reduced models such as SOLT[19] and HESEL,[45] which describe curvature-driven drift-interchange turbulence in the two-dimensional plane perpendicular to B at the outboard midplane. Indeed this is the expected character of resistive X-point modes: interchange-like in the midplane region and terminating near the X-point.[32]

Quantitative estimates for the SOL heat flux width, made both from Eq. (1) directly and using the scaling results expressed in Eq. (18), are roughly comparable to the minimum measured values of λ_q in NSTX. Remarkably, the normalized turbulent perpendicular heat flux, and hence λ_q can be expressed in the rather simple and general form of Eq. (15) assuming only the drift-interchange character of the turbulence. The numbers appearing in this expression (C_{dw}, C_{mhd} and $C_{k\rho}$) may be approximately universal. With the additional physical assumption that H mode turbulence is suppressed by ion pressure profile induced $E \times B$ flow shear, the even simpler form of Eq. (18) results. It is hoped that Eqs. (15) and (18) may provide a physics-based framework from which to approach future work in assessing turbulence effects on the SOL width.

Finally, SOLT code simulations were shown to capture some features of the experimental dataset. The simulations suggest that turbulence contributes to the physics that sets λ_q in NSTX. While it cannot be claimed that turbulence physics dominates λ_q the results of both the simulations and the estimates of Sec. V suggest that it is not negligible, at least for NSTX discharges with high plasma current. As pointed out here and in Ref. 27 this may have important, and potentially favorable, implications for future large R devices.

ACKNOWLEDGMENTS

This material is based upon work supported by the U.S. Department of Energy Office of Science, Office of Fusion Energy Sciences under Award Nos. DE-FG02-02ER54678 and DE-AC02-09CH11466. Basic theory contributions to the paper were also supported by the U.S. Department of Energy Office of Science, Office of Fusion Energy Sciences under Award No. DE-FG02-97ER54392. The authors are grateful to B. Davis, S. A. Sabbath and R. J. Maqueda for contributions to the GPI data analysis, to B. LeBlanc for Thomson scattering data and to R. Maingi, J.-W. Ahn, T. K. Gray and G. Canal for preparing discharge data used in the simulations. The digital data for this paper can be found at: http://arks.princeton.edu/ark:/88435/dsp018p58pg426.

[1]S. J. Zweben, J. A. Boedo, O. Grulke, C. Hidalgo, B. LaBombard, R. J. Maqueda, P. Scarin, and J. L. Terry, Plasma Phys. Controlled Fusion **49**, S1 (2007).
[2]G. R. Tynan, A. Fujisawa, and G. McKee, Plasma Phys. Controlled Fusion **51**, 113001 (2009).
[3]S. I. Krasheninnikov, D. A. D'Ippolito, and J. R. Myra, J. Plasma Phys. **74**, 679 (2008).
[4]D. A. D'Ippolito, J. R. Myra, and S. J. Zweben, Phys. Plasmas **18**, 060501 (2011).
[5]B. N. Rogers, J. F. Drake, and A. Zeiler, Phys. Rev. Lett. **81**, 4396 (1998).
[6]B. LaBombard, J. W. Hughes, N. Smick, A. Graf, K. Marr, R. McDermott, M. Reinke, M. Greenwald, B. Lipschultz, J. L. Terry, D. G. Whyte, S. J. Zweben, and A. C-Mod Team, Phys. Plasmas **15**, 056106 (2008).
[7]D. Carralero, G. Birkenmeier, H. W. Müller, P. Manz, P. deMarne, S. H. Müller, F. Reimold, U. Stroth, M. Wischmeier, E. Wolfrum, and The ASDEX Upgrade Team, Nucl. Fusion **54**, 123005 (2014).
[8]C. Bourdelle, L. Chôné, N. Fedorczak, X. Garbet, P. Beyer, J. Citrin, E. Delabie, G. Dif-Pradalier, G. Fuhr, A. Loarte, C. F. Maggi, F. Militello, Y.

Sarazin, L. Vermare, and JET Contributors, Nucl. Fusion **55**, 073015 (2015).
[9]O. E. Garcia, J. Horacek, and R. A. Pitts, Nucl. Fusion **55**, 062002 (2015).
[10]S. J. Zweben, W. M. Davis, S. M. Kaye, J. R. Myra, R. E. Bell, B. P. LeBlanc, R. J. Maqueda, T. Munsat, S. A. Sabbagh, Y. Sechrest, D. P. Stotler, and the NSTX Team, Nucl. Fusion **55**, 093035 (2015).
[11]S. J. Zweben, J. R. Myra, W. M. Davis, D. A. D'Ippolito, T. K. Gray, S. M. Kaye, B. P. LeBlanc, R. J. Maqueda, D. A. Russell, D. P. Stotler, and the NSTX-U Team, Plasma Phys. Controlled Fusion **58**, 044007 (2016).
[12]G. Birkenmeier, P. Manz, D. Carralero, F. M. Laggner, G. Fuchert, K. Krieger, H. Maier, F. Reimold, K. Schmid, R. Dux, T. Pütterich, M. Willensdorfer, E. Wolfrum, and The ASDEX Upgrade Team, Nucl. Fusion **55**, 033018 (2015).
[13]G. Fuchert, G. Birkenmeier, D. Carralero, T. Lunt, P. Manz, H. W. Müller, B. Nold, M. Ramisch, V. Rohde, U. Stroth, and the ASDEX Upgrade Team, Plasma Phys. Controlled Fusion **56**, 125001 (2014).
[14]J. A. Boedo, J. R. Myra, S. Zweben, R. Maingi, R. J. Maqueda, V. A. Soukhanovskii, J. W. Ahn, J. Canik, N. Crocker, D. A. D'Ippolito, R. Bell, H. Kugel, B. Leblanc, L. A. Roquemore, D. L. Rudakov, and NSTX Team, Phys. Plasmas **21**, 042309 (2014).
[15]P. Simon, M. Ramisch, A. A. Beletskii, A. Dinklage, M. Endler, S. Marsen, B. Nold, U. Stroth, P. Tamain, and R. Wilcox, Plasma Phys. Controlled Fusion **56**, 095015 (2014).
[16]J. R. Myra, D. A. Russell, D. A. D'Ippolito, J.-W. Ahn, R. Maingi, R. J. Maqueda, D. P. Lundberg, D. P. Stotler, S. J. Zweben, J. Boedo, M. Umansky, and NSTX Team, Phys. Plasmas **18**, 012305 (2011).
[17]D. A. Russell, D. A. D'Ippolito, J. R. Myra, B. LaBombard, J. L. Terry, and S. J. Zweben, Phys. Plasmas **19**, 082311 (2012).
[18]F. Militello, V. Naulin, and A. H. Nielsen, Plasma Phys. Controlled Fusion **55**, 074010 (2013).
[19]D. A. Russell, D. A. D'Ippolito, J. R. Myra, J. M. Canik, T. K. Gray, and S. J. Zweben, Phys. Plasmas **22**, 092311 (2015).
[20]B. I. Cohen, M. V. Umansky, W. M. Nevins, M. A. Makowski, J. A. Boedo, D. L. Rudakov, G. R. McKee, Z. Yan, and R. J. Groebner, Phys. Plasmas **20**, 055906 (2013).
[21]F. D. Halpern, P. Ricci, B. Labit, I. Furno, S. Jolliet, J. Loizu, A. Mosetto, G. Arnoux, J. P. Gunn, J. Horacek, M. Kocan, B. LaBombard, C. Silva, and JET-EFDA, Nucl. Fusion **53**, 122001 (2013).
[22]F. D. Halpern, P. Ricci, S. Jolliet, J. Loizu, and A. Mosetto, Nucl. Fusion **54**, 043003 (2014).
[23]J. Loizu, P. Ricci, F. D. Halpern, S. Jolliet, and A. Mosetto, Nucl. Fusion **54**, 083033 (2014).
[24]A. Y. Pankin, T. Rafiq, A. H. Kritz, G. Y. Park, C. S. Chang, D. Brunner, R. J. Groebner, J. W. Hughes, B. LaBombard, J. L. Terry, and S. Ku, Phys. Plasmas **22**, 092511 (2015).
[25]C. S. Chang, J. A. Boedo, R. Hager, S.-H. Ku, J. Lang, R. Maingi, D. Stotler, S. Zweben, and S. Parker, in Proceedings of the 25th IAEA Fusion Energy Conference, Saint Petersburg, Russia, 13–18 October 2014, Paper No. IAEA-CN-221/TH/2-3.
[26]M. Ono, S. M. Kaye, Y.-K. M. Peng, G. Barnes, W. Blanchard, M. D. Carter, J. Chrzanowski, L. Dudek, R. Ewig, D. Gates *et al.*, Nucl. Fusion **40**, 557 (2000).
[27]J. R. Myra, D. A. D'Ippolito, and D. A. Russell, Phys. Plasmas **22**, 042516 (2015).
[28]T. Eich, A. W. Leonard, R. A. Pitts, W. Fundamenski, R. J. Goldston, T. K. Gray, A. Herrmann, A. Kirk, A. Kallenbach, O. Kardaun *et al.*, Nucl. Fusion **53**, 093031 (2013).
[29]J. Horacek, R. A. Pitts, J. Adamek, G. Arnoux, J.-G. Bak, S. Brezinsek, M. Dimitrova, R. J. Goldston, J. P. Gunn, J. Havlicek *et al.*, Plasma Phys. Controlled Fusion **58**, 074005 (2016).
[30]J. W. Connor, G. F. Counsell, S. K. Erents, S. J. Fielding, B. LaBombard, and K. Morel, Nucl. Fusion **39**, 169 (1999).
[31]G. F. Counsell, J. W. Connor, S. K. Erents, A. R. Field, S. J. Fielding, B. La Bombard, and K. M. Morel, J. Nucl. Mater. **266–269**, 91 (1999).
[32]J. R. Myra, D. A. D'Ippolito, X. Q. Xu, and R. H. Cohen, Phys. Plasmas **7**, 2290 (2000).
[33]X. Q. Xu, R. H. Cohen, T. D. Rognlien, and J. R. Myra, Phys. Plasmas **7**, 1951 (2000).
[34]D. Farina, R. Pozzoli, and D. D. Ryutov, Nucl. Fusion **33**, 1315 (1993).
[35]J. L. Terry, S. J. Zweben, M. V. Umansky, I. Cziegler, O. Grulke, B. LaBombard, and D. P. Stotler, J. Nucl. Mater. **390–391**, 339 (2009).
[36]R. J. Maqueda, D. P. Stotler, and the NSTX Team, Nucl. Fusion **50**, 075002 (2010).
[37]O. Grulke, J. L. Terry, I. Cziegler, B. LaBombard, and O. E. Garcia, Nucl. Fusion **54**, 043012 (2014).
[38]T. K. Gray, J. M. Canik, R. Maingi, A. G. McLean, J.-W. Ahn, M. A. Jaworkski, R. Kaita, M. Ono, S. F. Paul, and NSTX Team, Nucl. Fusion **54**, 023001 (2014).
[39]R. J. Goldston, Nucl. Fusion **52**, 013009 (2012).
[40]B. N. Rogers and W. Dorland, Phys. Plasmas **12**, 062511 (2005).
[41]P. Ricci, B. N. Rogers, and S. Brunner, Phys. Rev. Lett. **100**, 225002 (2008).
[42]J. R. Myra, D. A. D'Ippolito, D. A. Russell, M. V. Umansky, and D. A. Baver, J. Plasma Phys. **82**, 905820210 (2016).
[43]J. R. Myra, D. A. Russell, D. A. D'Ippolito, J.-W. Ahn, R. Maingi, R. J. Maqueda, D. P. Lundberg, D. P. Stotler, S. J. Zweben, and M. Umansky, J. Nucl. Mater. **415**, S605 (2011).
[44]T. K. Gray, private communication (2016).
[45]J. J. Rasmussen, A. H. Nielsen, J. Madsen, V. Naulin, and G. S. Xu, Plasma Phys. Controlled Fusion **58**, 014031 (2015).